Supplementary Information

Tuning scalar spin chirality in ultrathin films of the kagome-lattice ferromagnet Fe_3Sn

Kohei Fujiwara[1*], Yasuyuki Kato[2], Takeshi Seki[1,3], Kentaro Nomura[1,3], Koki Takanashi[1,3,4], Yukitoshi Motome[2], and Atsushi Tsukazaki[1,3,4]

[1]*Institute for Materials Research, Tohoku University, Sendai 980-8577, Japan*

[2]*Department of Applied Physics, University of Tokyo, Tokyo 113-8656, Japan*

[3]*Center for Spintronics Research Network (CSRN), Tohoku University, Sendai 980-8577, Japan*

[4]*Center for Science and Innovation in Spintronics (CSIS), Core Research Cluster, Tohoku University, Sendai 980-8577, Japan*

[*]Author to whom correspondence should be addressed: kohei.fujiwara@tohoku.ac.jp

Supplementary Figures

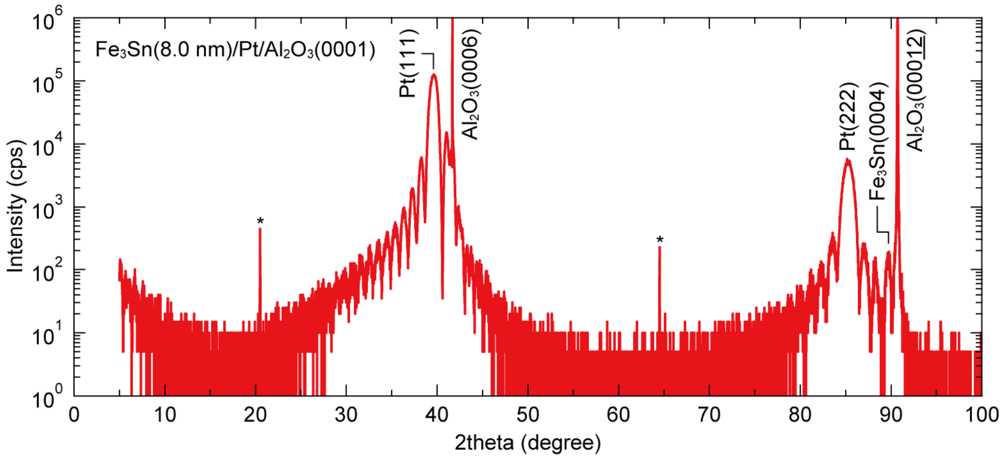

Supplementary Figure 1. Out-of-plane X-ray diffraction pattern of a 8.0-nm-thick $Fe_3Sn/Pt/Al_2O_3(0001)$ sample analyzed by TEM. Although the $Fe_3Sn(0002)$ peak at $2\theta \sim 41°$ overlaps with the strong Pt(111) peak and the associated thickness fringes, the $Fe_3Sn(0004)$ peak is discerned at $2\theta = 89.8°$. Asterisks indicate forbidden reflections of Al_2O_3.

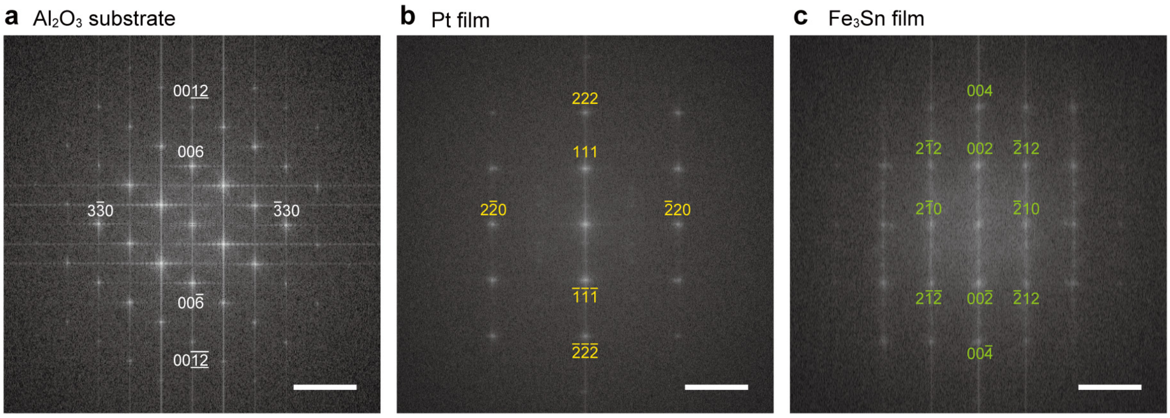

Supplementary Figure 2. Fast Fourier transformation (FFT) diffraction patterns calculated from the TEM image shown in Fig. 1d. a,b,c, The Al_2O_3 substrate, Pt film, and Fe_3Sn film regions, respectively. Scale bar, 5 nm^{-1}. The result of (c) is consistent with the high-temperature Fe_3Sn phase (JCPDS PDF 01-074-5857).

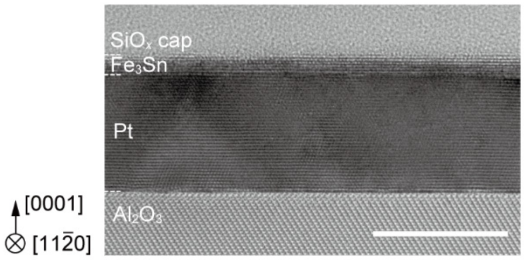

Supplementary Figure 3. Cross-sectional TEM image of a Fe_3Sn/Pt bilayer sample with t = 1.6 nm viewed along $Al_2O_3[11\bar{2}0]$. Scale bar, 10 nm.

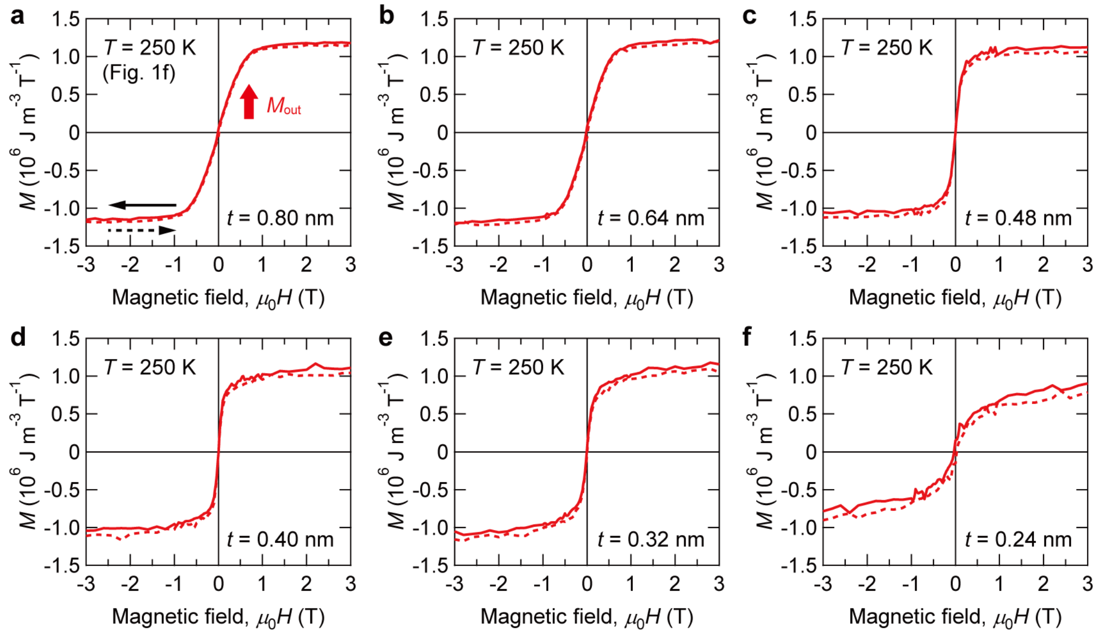

Supplementary Figure 4. $\boldsymbol{M}$ **versus** $\boldsymbol{\mu_0 H}$ **curves of** $\mathbf{Fe_3Sn}$**/Pt bilayer samples measured in an out-of-plane** $\boldsymbol{H}$**.** Typical data taken at $T = 250$ K are shown. **a,** $t = 0.80$ nm, **b,** $t = 0.64$ nm, **c,** $t = 0.48$ nm, **d,** $t = 0.40$ nm, **e,** $t = 0.32$ nm, and **f,** $t = 0.24$ nm. The data for $t = 0.80$ nm are replotted from Fig. 1f. The red solid and dashed curves correspond to the decreasing-field and increasing-field branches, as shown by the black solid and dashed arrows, respectively.

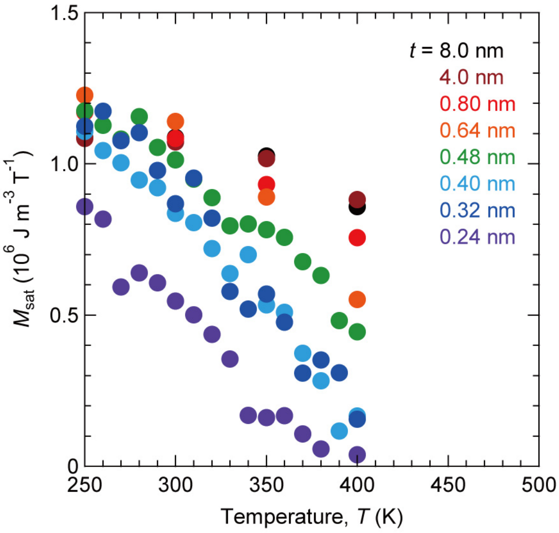

Supplementary Figure 5. ***T*** **dependence of** M_{sat} **for** Fe_3Sn**/Pt bilayer samples with** ***t*** **= 8.0–0.24 nm.**

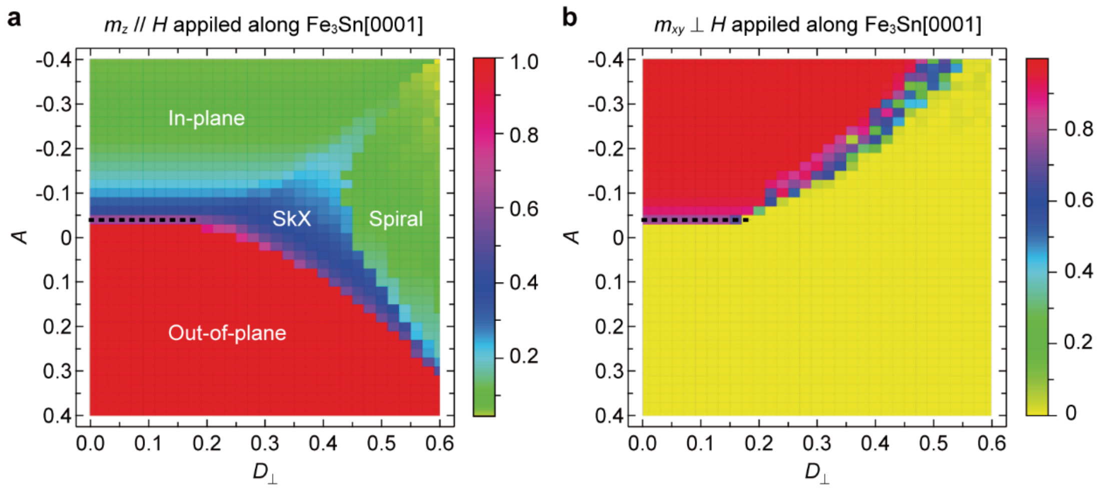

Supplementary Figure 6. Simulation results of magnetic moments in Fe_3Sn single layer. a, Out-of-plane magnetization component m_z, **b,** in-plane magnetization component m_{xy} in an magnetic field *H* applied along the out-of-plane Fe_3Sn[0001] direction. Dotted lines indicate the boundary between the in-plane and out-of-plane phases. Typical spin textures in the SkX and spiral phases are shown in Supplementary Fig. 7.

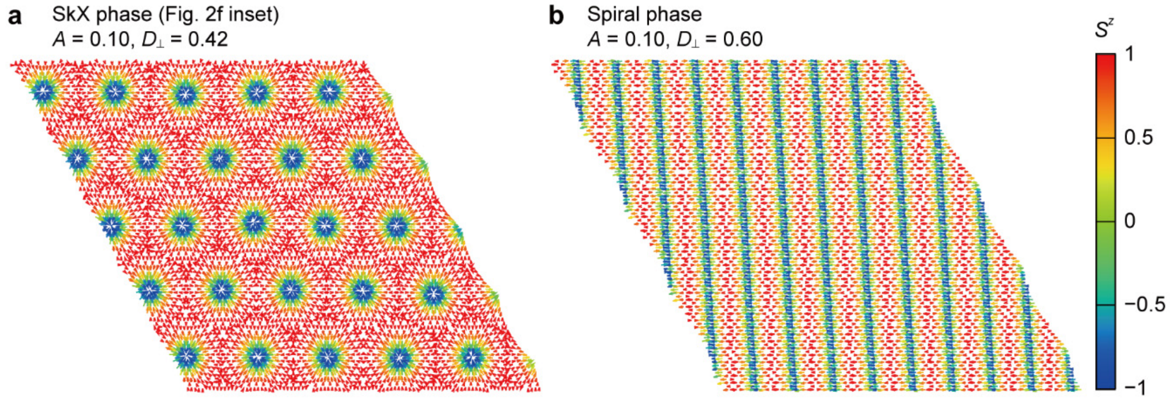

Supplementary Figure 7. Simulation results of spin textures in Fe_3Sn single layer. a, The SkX phase obtained with A = 0.10 and $D_\perp$ = 0.42 (magnified image of Fig. 2f inset). **b,** The spiral phase obtained with A = 0.10 and $D_\perp$ = 0.60. The color corresponds to S^z of each spin. The integrated spin solid angle $|\Omega_{\mathrm{tot}}|$ becomes finite in the SkX phase but becomes zero in the spiral phase (Fig. 2f).

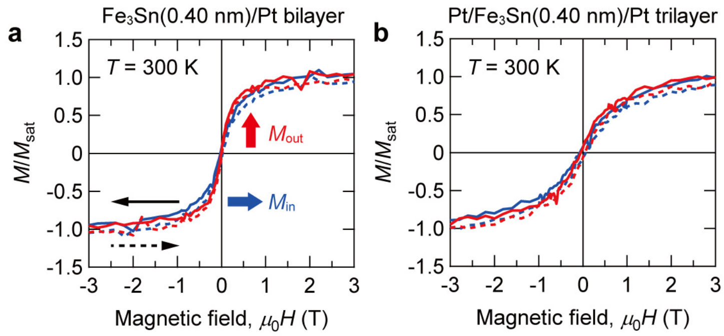

Supplementary Figure 8. Normalized magnetization M/M_{sat} versus $\mu_0 H$ curves. a, Fe_3Sn(0.40 nm)/Pt thin-bilayer and **b,** Fe_3Sn(0.40 nm)/Pt thin-trilayer structures measured in out-of-plane and in-plane H configurations at $T = 300$ K. The solid and dashed curves correspond to the decreasing-field and increasing-field branches, as shown by the black solid and dashed arrows, respectively.

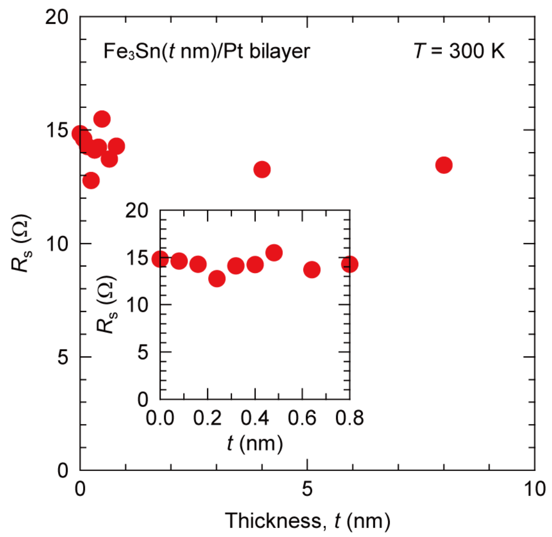

Supplementary Figure 9. *t* dependence of sheet resistance R_s at $T = 300$ K in Fe_3Sn/Pt bilayer samples. The inset shows the data for $t = 0$–0.80 nm. Using the data for $t = 0$ nm (bare 10-nm-thick Pt without Fe_3Sn), the electrical resistivity of Pt is calculated to be 1.48×10^{-5} Ω cm. The virtually *t*-independent R_s indicates that the 10-nm-thick Pt bottom layer is significantly more conductive than the Fe_3Sn layer.

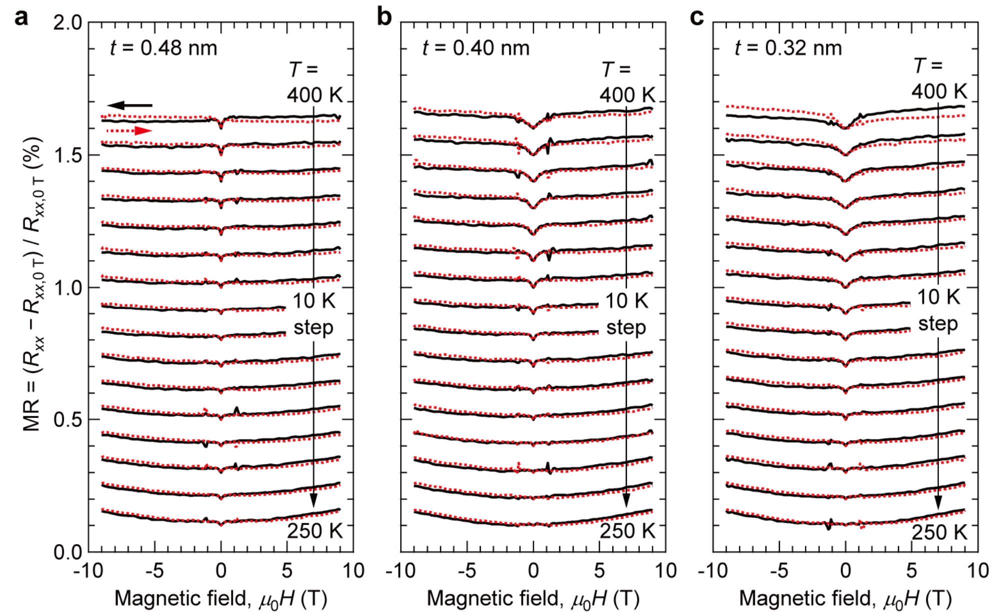

Supplementary Figure 10. Magnetoresistance MR versus $\mu_0 H$ curves at varied *T*. Fe_3Sn(t nm)/Pt bilayer samples with **a,** t = 0.48 nm, **b,** t = 0.40 nm, and **c,** t = 0.32 nm. MR is defined as $\mathrm{MR} = \frac{R_{xx} - R_{xx,0\,\mathrm{T}}}{R_{xx,0\,\mathrm{T}}}$, where R_{xx} is the longitudinal resistance at a given field and $R_{xx,0\,\mathrm{T}}$ is that at $\mu_0 H = 0$ T. The R_{xx} was simultaneously measured with R_{yx} upon decreasing $\mu_0 H$ from 9 T to −9 T and increasing $\mu_0 H$ from −9 T to 9 T. By symmetrizing the decreasing-field and increasing-field R_{xx} data, the symmetrized MR curves were obtained. The two curves corresponding to the decreasing-field and increasing-field scans are shown, which are represented by black solid and red dotted curves, respectively. The data are shifted vertically for clarity. The MR is as small as 0.1%. The spike-like behavior at about ±1 T might be associated with the change in the field-sweep rate at ±1 T.

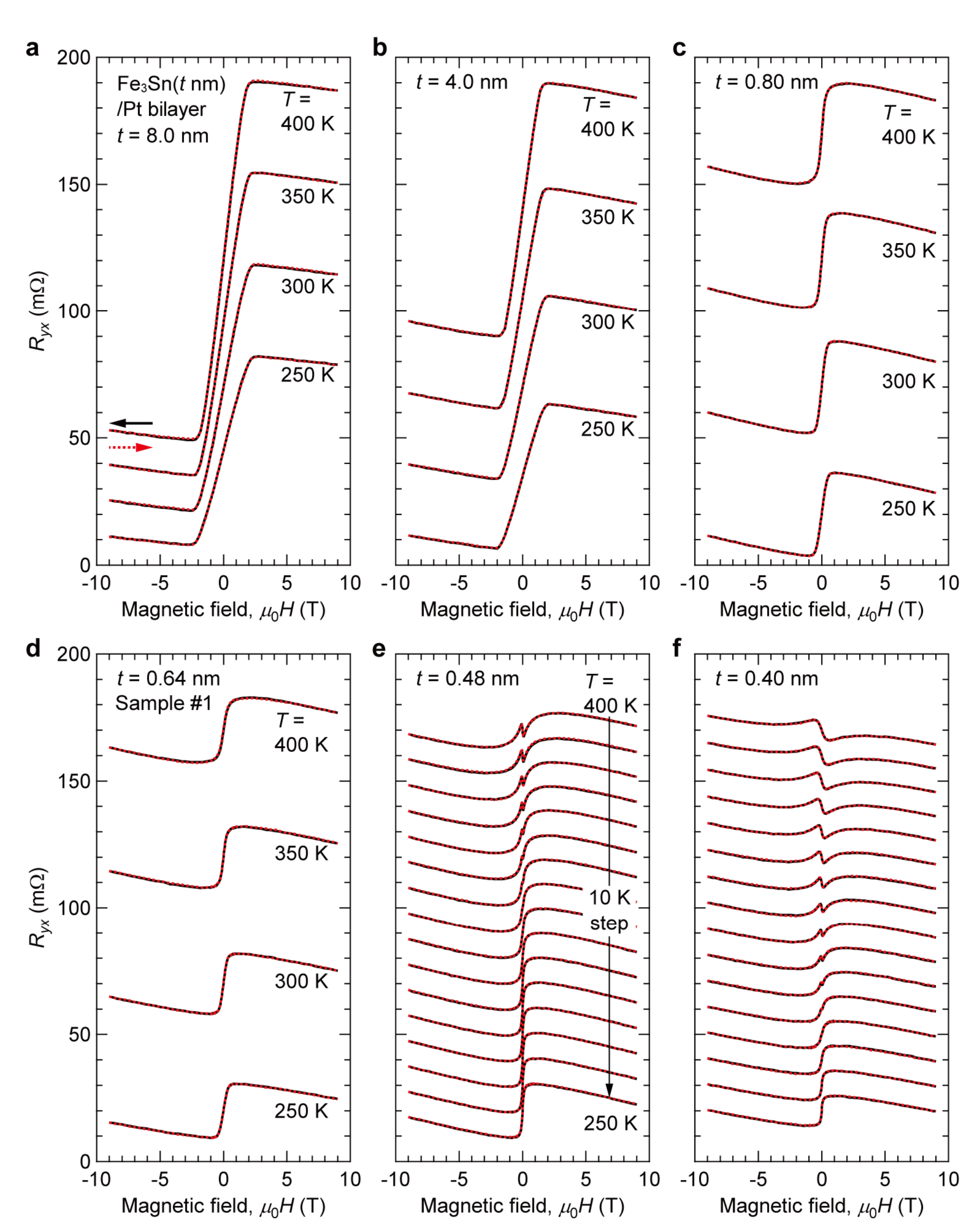

Supplementary Figure 11. R_{yx} versus $\mu_0 H$ curves at varied *T*. The two curves corresponding to the decreasing-field and increasing-field scans are shown, which are represented by black solid and red dotted curves, respectively. The data are shifted vertically for clarity. Fe_3Sn(*t* nm)/Pt bilayer samples with **a,** *t* = 8.0 nm, **b,** *t* = 4.0 nm, **c,** *t* = 0.80 nm, **d,** *t* = 0.64 nm (sample #1), **e,** *t* = 0.48 nm, and **f,** *t* = 0.40 nm.

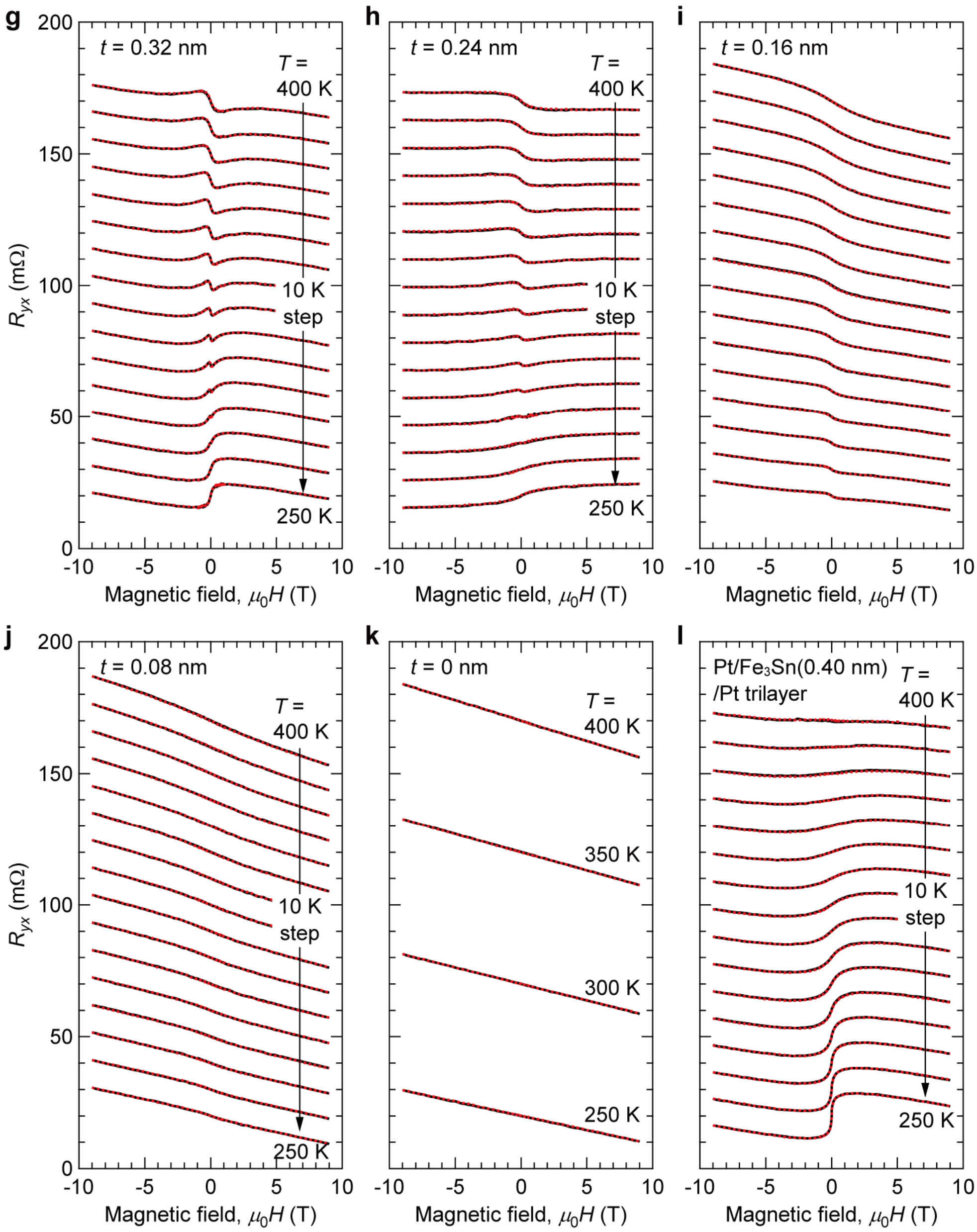

(Continued) Supplementary Figure 11. g, t = 0.32 nm, **h,** t = 0.24 nm, **i,** t = 0.16 nm, **j,** t = 0.08 nm, and **k,** t = 0 nm (Pt monolayer). **l,** Pt/Fe_3Sn(t = 0.40 nm)/Pt trilayer. The AHE behavior is very similar to that of a Fe_3Sn(t = 0.40 nm)/Pt bilayer (Supplementary Fig. 11f) but no THE-like responses occur at all measured T.

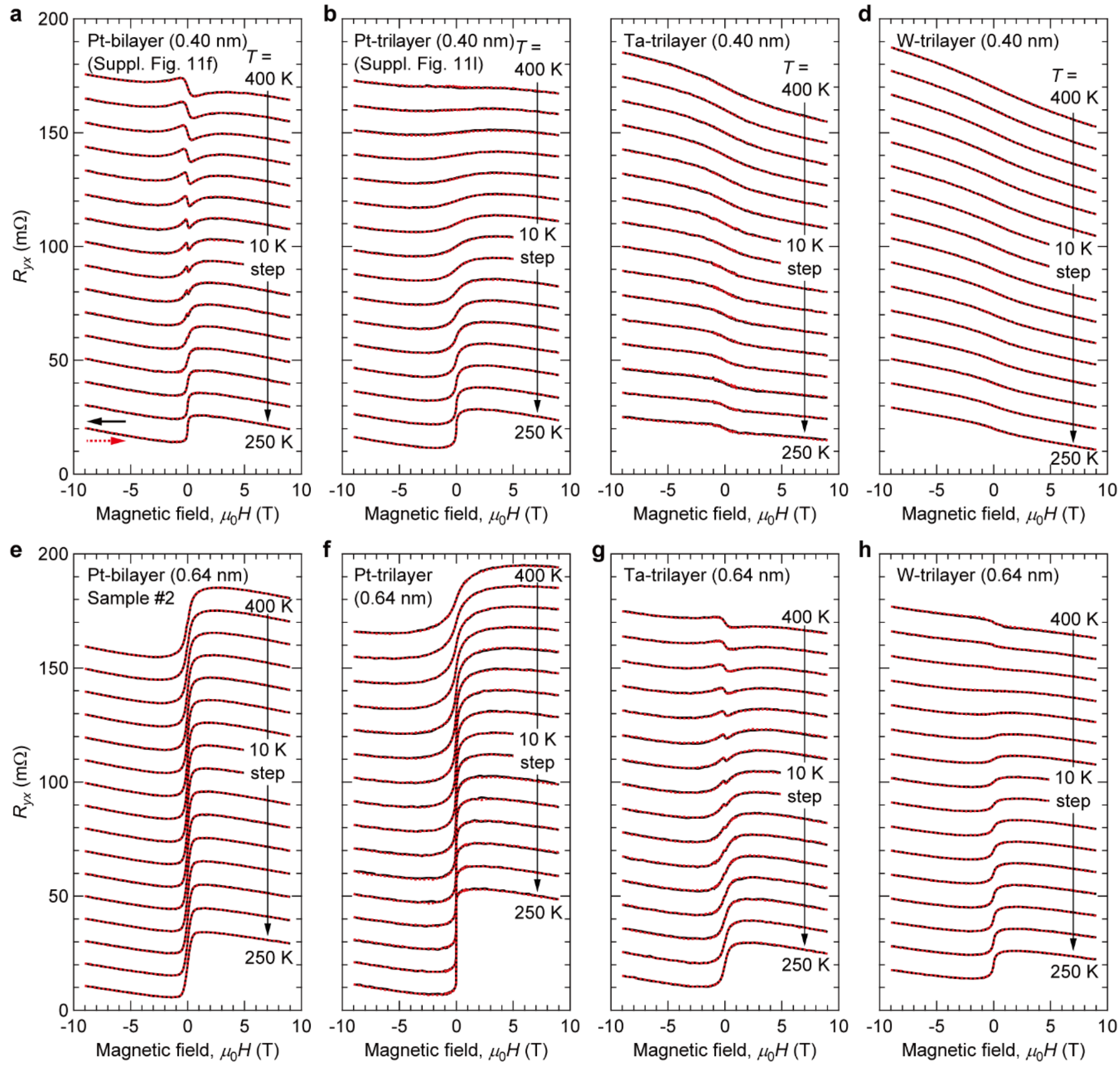

Supplementary Figure 12. $\boldsymbol{R_{yx}}$ **versus** $\boldsymbol{\mu_0 H}$ **curves at varied** $\boldsymbol{T}$**.** The two curves corresponding to the decreasing-field and increasing-field scans are shown, which are represented by black solid and red dotted curves, respectively. The data are shifted vertically for clarity. **a,** Fe_3Sn(t nm)/Pt bilayer (Pt-bilayer), **b,** symmetric Pt/Fe_3Sn/Pt trilayer (Pt-trilayer), **c,** asymmetric Ta/Fe_3Sn/Pt trilayer (Ta-trilayer), **d,** asymmetric W/Fe_3Sn/Pt trilayer (W-trilayer) samples with t = 0.40 nm, **e,** Fe_3Sn/Pt bilayer, **f,** symmetric Pt/Fe_3Sn/Pt trilayer, **g,** asymmetric Ta/Fe_3Sn/Pt trilayer, **h,** asymmetric W/Fe_3Sn/Pt trilayer samples with t = 0.64 nm.

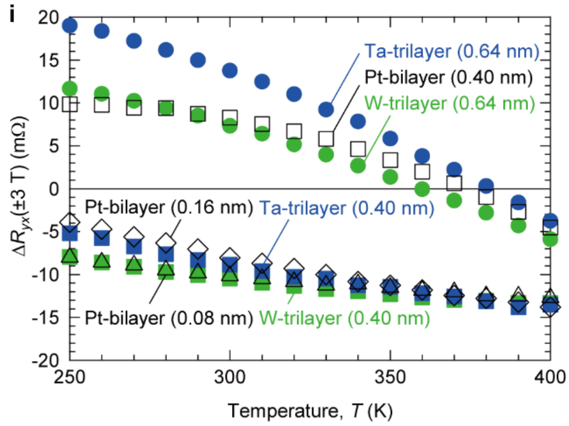

(Continued) Supplementary Figure 12. i, T dependence of $\Delta R_{yx}(\pm 3\ \mathrm{T})$. See Supplementary Note 1 for the explanations about these results.

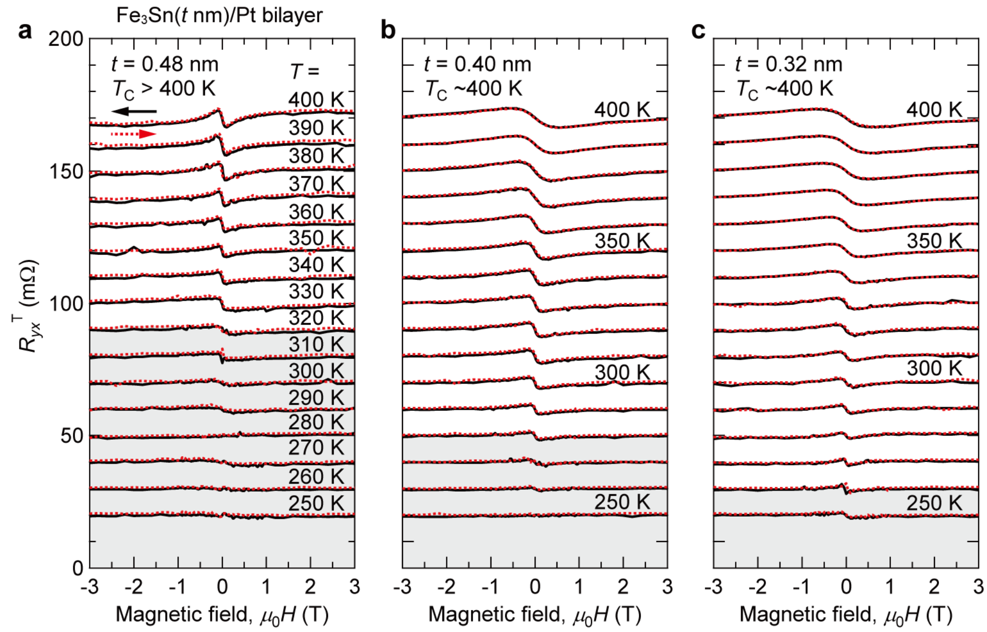

Supplementary Figure 13. a,b,c, R_{yx}^{T} versus $\mu_0 H$ curves obtained by analyzing the data shown in Figs. 4a, b, and c, respectively. The two curves corresponding to the decreasing-field and increasing-field scans are shown, which are represented by black solid and red dotted curves, respectively. The data are shifted vertically for clarity. The grey-shaded regions represent the T range where no clear THE signals are discerned; THE-like behavior may also be seen at T = 320 K for t = 0.48 nm, T = 280 K for t = 0.40 nm, and T = 260 K for t = 0.32 nm. We focused on the data showing clear humps both in the raw R_{yx} and the analyzed R_{yx}^{T} in the discussion of THE.

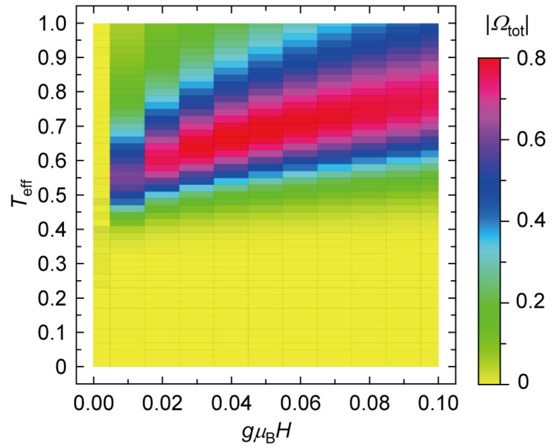

Supplementary Figure 14. Simulated $|\Omega_{tot}|$ as a function of $g\mu_B H$ and T_{eff}. The simulation conditions are the same to that used for Fig. 4f.

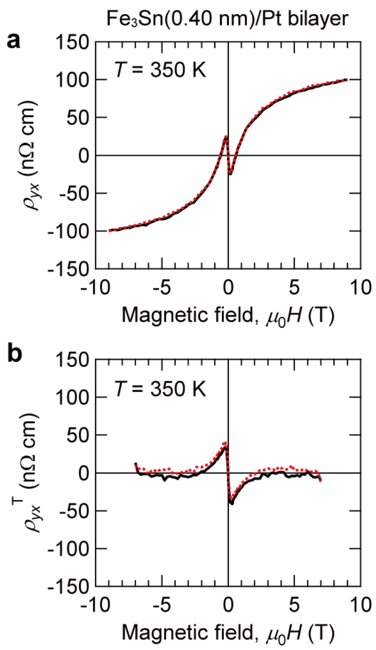

Supplementary Figure 15. Calculation of topological Hall resistivity ρ_{yx}^{T}. a, Hall resistivity ρ_{yx} of the Fe_3Sn layer. For the analysis, the data of the Fe_3Sn(t = 0.40 nm)/Pt bilayer and reference Pt monolayer samples at T = 350 K shown in Supplementary Figs. 11f and 11k were used. **b,** Calculated ρ_{yx}^{T}. The ρ_{yx}^{T} was calculated by subtracting the ordinary Hall resistivity $R_0\mu_0H$ and anomalous Hall resistivity (proportional to M) components from the ρ_{yx}. The two curves corresponding to the decreasing-field and increasing-field scans are shown, which are represented by black solid and red dotted curves, respectively.

Supplementary Table

Supplementary Table 1. $\left|\rho_{yx}^{\mathrm{T}}\right|$, R_0, $n_{\mathrm{sk}}^{-0.5}$, **the temperature where THE appears (** T_{THE} **).** The data were taken from the data of interface systems in literatures. $\rho_{yx}^{\mathrm{T}} = PR_0 n_{\mathrm{sk}} \phi_0$

Interface	$\left\|\rho_{yx}^{\mathrm{T}}\right\|$ (μΩ cm)	R_0 (cm^3 C^{-1})	$n_{\mathrm{sk}}^{-0.5}$ (nm)	T_{THE} (K)	Suppl. Ref.
$SrRuO_3/SrIrO_3$	0.10–1.1	6.6–8.1 × 10^{-4}	4.7–15	5–120	1
MnGa/Pt(5 nm)	1.2 at 300 K	8.57 × 10^{-3}	35 at 300 K	5–300	2
MnGa/Ta(5 nm)	2.7 at 300 K	1.33 × 10^{-3}	10 at 300 K	5–300	2
Ir/Fe/Co/Pt	0.0042 at 300 K	−6.2 × 10^{-5}	270 at 300 K	5–300	3
Fe_3Sn(0.40 nm)/Pt	0.037 at 350 K	8.48 × 10^{-5}	9.68–30.6 at 350 K	290–400	This work

Supplementary Note

Supplementary Note 1:

Asymmetric Ta (2 nm)/Fe_3Sn (t nm)/Pt (10 nm) and W (2 nm)/Fe_3Sn (t nm)/Pt (10 nm) trilayer structures (t-nm-thick Ta-trilayer and W-trilayer) were fabricated on Al_2O_3(0001) substrates. The Ta and W capping layers were deposited at the substrate temperature of 100 ºC, which is the same condition for the deposition of Pt capping layer. The topmost surfaces were capped with SiO_x (15 nm) layers as in the Fe_3Sn (t nm)/Pt bilayer and symmetric Pt/Fe_3Sn (t nm)/Pt trilayer structures (t-nm-thick Pt-bilayer and Pt-trilayer). In Supplementary Fig. 12, we compare the Pt-bilayer and trilayer structures with identical t values (see (a)–(d) for t = 0.40 nm and (e)–(h) for t = 0.64 nm). In (c,d) the 0.40-nm-thick Ta- and W-trilayer structures, AHE is not obvious even at T = 250 K; the overall behavior looks those of the 0.16- or 0.08-nm-thick Pt-bilayer structures (see the panel (i)). In the thicker (g,h) 0.64-nm-thick Ta- and W-trilayer structures, AHE occurs clearly; the magnitude and T dependence are closer to those of (a) the 0.40-nm-thick Pt-bilayer and (b) 0.40-nm-thick Pt-trilayer structures rather than (e) the 0.64-nm-thick Pt-bilayer and (f) 0.64-nm-thick Pt-trilayer structures. These results indicate that the effective Fe_3Sn thickness in the Ta- and W-trilayer structures is reduced by approximately 0.2–0.3 nm as compared with the cases using SiO_x and Pt capping layers. Interdiffusion might be more significant at the interfaces of Ta/Fe_3Sn and W/Fe_3Sn. Taking into account the reduced effective Fe_3Sn thickness, we focused on the 0.64-nm-thick Ta-and W-trilayer structures as the control samples of the 0.40-nm-thick Pt-bilayer and 0.40-nm-thick Pt-trilayer structures for which the occurrence of THE by the interfacial DMI is discussed in the manuscript.

In the 0.64-nm-thick Ta-trilayer structure, R_{yx} humps (R_{yx}^{T}) appear at low $\mu_0 H$ in the range of T = 300–400 K. In the 0.64-nm-thick W-trilayer structure, no clear humps are detected except for T = 400 K. These results can be explained by considering the different strengths of interfacial DMI at the top and bottom interfaces. It has been reported that the interfacial DMI of W for Fe [A. Belabbes *et al.*, *Phys. Rev. Lett.* **117**, 247202 (2016)] and CoFeB [I. Gross *et al.*, *Phys. Rev. B* **94**, 064413 (2016)] is as strong as that of Pt and has the same sign. Hence, as in the symmetric Pt/Fe_3Sn/Pt trilayer structure, the opposite interfacial DMI contributions from the top W/Fe_3Sn and bottom Fe_3Sn/Pt interfaces in the W/Fe_3Sn/Pt trilayer structure are expected to suppress each other. On the other hand, the interfacial DMI of Ta is known to be much weaker than Pt [A. Casiraghi *et al.*, *Commun. Phys.* **2**, 145 (2019)]. In the Ta/Fe_3Sn/Pt trilayer structure, the effective interfacial DMI should be governed by the large contribution from the bottom Fe_3Sn/Pt interface. Therefore, these results add further support for the interfacial DMI origin of the observed THE.

Supplementary References

1. Matsuno, J. *et al.* Interface-driven topological Hall effect in $SrRuO_3$-$SrIrO_3$ bilayer. *Sci. Adv.* **2**, e1600304 (2016).
2. Meng, K. *et al*. Robust emergence of a topological Hall effect in MnGa/heavy metal bilayers. *Phys. Rev. B* **97**, 060407(R) (2018).
3. Raju, M. *et al.* The evolution of skyrmions in Ir/Fe/Co/Pt multilayers and their topological Hall signature. *Nat. Commun.* **10**, 696 (2019).
4. Belabbes, A., Bihlmayer, G., Bechstedt, F., Blügel, S. & Manchon, A. Hund's Rule-Driven Dzyaloshinskii-Moriya Interaction at 3*d*-5*d* Interfaces. *Phys. Rev. Lett.* **117**, 247202 (2016).
5. Gross, I. *et al*. Direct measurement of interfacial Dzyaloshinskii-Moriya interaction in *X*|CoFeB|MgO heterostructures with a scanning NV magnetometer (*X*=Ta, TaN, and W). *Phys. Rev. B* **94**, 064413 (2016).
6. Casiraghi, A. *et al*. Individual skyrmion manipulation by local magnetic field gradients. *Commun. Phys.* **2**, 145 (2019).